

Evaluation of terrain effects in AEM surveys using the boundary element method

Guimin Liu* and Alex Becker‡

ABSTRACT

In mountainous areas, electromagnetic terrain effects are readily observed in the course of VLF (14-20 kHz) measurements made on the surface and constitute a serious source of geological noise that affects the collected data. One may, therefore, inquire whether similar effects will be observed during the course of conventional helicopter-towed electromagnetic (HEM) surveys as the frequency of the newer systems is increased beyond the lower regions of the audio range. To answer the question, we have evaluated the terrain effects that would be observed with a conventional HEM system in a number of simple cases. The operating

frequency chosen for most of the numerical simulations was 8 kHz, while the topographic features investigated were taken to be two-dimensional. The calculations were done using the boundary element method of solving the appropriate integral equations. Accuracy of the numerical solutions was shown to vary from 1 percent for a half space to 10 percent for a shallow valley where the verification was done on a laboratory scale model. For the models investigated, the amplitude of the computed secondary fields shows a distinct correlation with the overflown topography. Surprisingly, however, the phase of the secondary field remains invariant and so may be reliably used to compute the resistivity of the terrain below the aircraft.

INTRODUCTION

Terrain effects can be an important factor in any geophysical survey. They are of course most evident in gravity data and less so in magnetic data. They are not, however, usually observed in electromagnetic data and were, until recently, of no concern to the geophysicist who used electromagnetics for mineral exploration. Because of the high audio frequencies involved, electromagnetic terrain effects were first noticed in VLF data acquired in mountainous areas (Whittles, 1969; Harrison et al., 1971; Arcone, 1978). Further work on this topic by Karous (1979) and Eberle (1981) offered a simple explanation for the observed terrain related VLF anomalies. These could be accounted for by applying Ampere's Law to an assumed uniform current concentration in a topographic protrusion (Karous, 1979) or, in special cases, by simply considering the reflection of plane waves from an inclined surface (Eberle, 1981).

Neither one of these methods allows the prediction of topographic effects for a closely coupled electromagnetic

system such as is routinely used in ground and airborne electromagnetic (AEM) surveys. Typically, these surveys are usually done in the lower audio range (0.3-3 kHz) and such effects are not observed often. The use of electromagnetics however, was recently expanded from mineral exploration to encompass geological mapping related to environmental, geohydrological, and geotechnical problems (Fraser, 1978). Accordingly, conventional EM equipment was enhanced to operate over a much wider frequency range (Fraser, 1979) so that at this point operation frequencies up to 60 kHz are available. One can thus expect that terrain effects will now be observed more commonly.

The objective here is to numerically evaluate the topographic effects in an AEM survey using the boundary element method (Brebbia et al., 1984). For eddy current problems, the theory of deriving the coupled boundary integral equations was given by Mayergoyz (1982). These equations have been known for some time in EM literature, yet no numerical results appear to have been presented based on this formulation. Here we transform the pertinent

Presented at the 60th Annual International Meeting, Society of Exploration Geophysicists. Manuscript received by the Editor September 10, 1990; revised manuscript received August 2, 1991.

*Formerly CGER, Macquarie University, NSW 2109, Australia; presently BHP Research-ML, 245 Wellington Rd., Mulgrave, VIC 3170, Australia.

‡Dept. of Materials Science and Mineral Engineering, University of California, Berkeley, California 94720.

© 1992 Society of Exploration Geophysicists. All rights reserved.

equations in the strike direction for two-dimensional (2-D) topography, and then solve the transformed equations numerically. Although in some aspects this work resembles that of Doherty (1988) or that of Parry and Ward (1971), it differs in the underlying principle used to derive the boundary integral equations. Furthermore, since in our case the EM field in the air is quasi-static, a scalar potential suffices to describe the magnetic field. The resulting boundary integral equations involve 25 percent fewer unknowns than used by Doherty so that the numerical computation is considerably faster. Numerical results for common topographic features such as an escarpment, a valley, and a hill will be shown following the presentation of the theory.

MATHEMATICAL FORMULATION

Consider an alternating electric current loop (magnetic dipole) in the air above a conductive homogeneous ground with arbitrary surface relief as shown in Figure 1. In the case examined, the height of the source over the ground is small compared with the wave length so that the electromagnetic fields in question are quasi-static. The secondary magnetic field in the air can be represented by an integral of fictitious magnetic charges ξ distributed on the ground surface S . Similarly, the magnetic field in the earth can be represented by an integral of fictitious electric currents \mathbf{J} distributed on

the ground surface. From the continuity conditions for the magnetic field, it can be shown that the charges and currents satisfy the following coupled equations (Mayergoyz, 1982)

$$\mathbf{J}(M) + \frac{1}{2\pi} \int_S \mathbf{n} \times \left(\mathbf{J}(P) \times \nabla \frac{e^{-ikr}}{r_{PM}} \right) ds - \frac{1}{2\pi} \int_S \xi(P) \mathbf{n} \times \nabla \frac{1}{r_{PM}} ds = -\frac{1}{2\pi} \mathbf{n} \times \mathbf{H}_p(M), \quad (1)$$

$$\xi(M) - \frac{1}{2\pi} \int_S \xi(P) \mathbf{n} \cdot \nabla \frac{1}{r_{PM}} ds + \frac{1}{2\pi} \frac{\mu}{\mu_0} \int_S \mathbf{n} \cdot \left(\mathbf{J}(P) \times \nabla \frac{e^{-ikr}}{r_{PM}} \right) ds = -\frac{1}{2\pi} \mathbf{n} \cdot \mathbf{H}_p(M). \quad (2)$$

Here \mathbf{n} is the unit normal at a field point M on ground surface S ; \mathbf{H}_p is the primary magnetic field at M ; the gradient operator ∇ is for the field point M . The magnetic permeability of the ground is μ , and μ_0 is that of free space. All the integrals in equations (1) and (2) are in the sense of the Cauchy principal value. Once the charges are obtained, the secondary magnetic field at point O in the air can be computed by,

$$\mathbf{H}_s = \int_S \frac{\xi(P)}{r_{PO}^3} \mathbf{r}_{PO} ds. \quad (3)$$

Equations (1) and (2) have been known for some time in the electromagnetic literature on eddy currents, yet no numerical results appear to have been presented based on this formulation.

In the special case when the lower medium is highly conductive, equations (1) and (2) reduce to a single equation,

$$\xi(M) - \frac{1}{2\pi} \int_S \xi(P) \mathbf{n} \cdot \nabla \frac{1}{r_{PM}} ds = -\frac{1}{2\pi} \mathbf{n} \cdot \mathbf{H}_p(M). \quad (4)$$

This special case has been previously considered by Liu and Becker (1990).

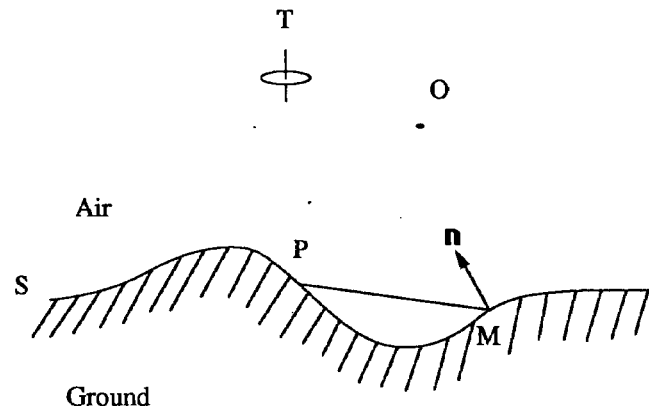


FIG. 1. Geometry for the boundary-value problem.

TABLE OF SYMBOLS

| | |
|--|---|
| $\mathbf{H}_s, H_{sx}, H_{sz}$ | Secondary magnetic field and its x - and z -components |
| $\mathbf{H}_p, H_{px}, H_{py}, H_{pz}$ | Primary magnetic field and its components |
| \mathbf{J}, J_s, J_y | Fictitious surficial electric current density and its tangential (in x - z plane) and y -components |
| ξ | fictitious magnetic charge density |
| $\hat{x}, \hat{y}, \hat{z}$ | unit vectors along x , y , and z directions |
| S | ground surface |
| M | a point on S |
| P | point of integration on S |
| O | a point above S |
| $\mathbf{n}, n_x, n_y, n_z$ | outward unit normal at M and its components |
| r_{PM} | distance from P to M |
| r_{PO} | distance from P to O |
| $\rho = r_{PM} _{y=0}$ | |
| t | ground surface relief |
| μ | magnetic permeability of ground |
| μ_0 | magnetic permeability of free space |
| σ | electrical conductivity of ground |
| f | frequency of system operation |
| $\omega = 2\pi f$ | |
| $i = \sqrt{-1}$ | |
| $k = \sqrt{-i\omega\mu\sigma}$ | propagation constant |
| k_y | wavenumber along the strike direction |
| $v^2 = k_y^2 - k^2$ | |
| K_0 | modified Bessel function of the second kind of order 0 |
| K_1 | modified Bessel function of the second kind of order 1 |
| θ | angle of the tangential at P |

The above formulation is valid for any general 3-D surface relief. Now consider the case when the conducting medium includes a 2-D feature that strikes in the y -direction. The surface relief of the ground can then be described by a function of x , i.e., $t(x)$. In this case, the integration along the y -direction implied in the previous surface integrals is a convolution of the charges or currents with a geometric kernel. Taking the Fourier transform of equations (1) and (2) with regard to y results in

$$\begin{aligned} \mathbf{J}(x, k_y) + \frac{1}{2\pi} \int_{-\infty}^{+\infty} \mathbf{n} \times (\mathbf{J}(x', k_y) \times \mathbf{U}) dx' \\ - \frac{1}{2\pi} \int_{-\infty}^{+\infty} \xi(x', k_y) \mathbf{n} \times \mathbf{V} dx' \\ = -\frac{1}{2\pi} \mathbf{n} \times \mathbf{H}_p(x, k_y), \end{aligned} \quad (5)$$

$$\begin{aligned} \xi(x, k_y) - \frac{1}{2\pi} \int_{-\infty}^{+\infty} \xi(x', k_y) \mathbf{n} \cdot \mathbf{V} dx' \\ + \frac{1}{2\pi} \frac{\mu}{\mu_0} \int_{-\infty}^{+\infty} \mathbf{n} \cdot (\mathbf{J}(x, k_y) \times \mathbf{U}) dx' \\ = -\frac{1}{2\pi} \mathbf{n} \cdot \mathbf{H}_p(x, k_y). \end{aligned} \quad (6)$$

Here,

$$\begin{aligned} \mathbf{U} = -\frac{2\nu\sqrt{1+[dt(x')/dx']^2}}{\rho} \{\hat{\mathbf{x}}(x-x') \\ + \hat{\mathbf{z}}[t(x)-t(x')]\} K_1(\rho\nu) + \hat{\mathbf{y}}2ik_y K_0(\rho\nu), \\ \mathbf{V} = -\frac{2|k_y|\sqrt{1+[dt(x')/dx']^2}}{\rho} \{\hat{\mathbf{x}}(x-x') \\ + \hat{\mathbf{z}}[t(x)-t(x')]\} K_1(\rho|k_y|) + \hat{\mathbf{y}}2ik_y K_0(\rho|k_y|). \end{aligned} \quad (8)$$

In these equations, k_y is the wavenumber in the y -direction, $\nu = \sqrt{k_y^2 + i\omega\mu\sigma}$, $\hat{\mathbf{x}}$, $\hat{\mathbf{y}}$, and $\hat{\mathbf{z}}$ are the unit vectors in the direction of x , y , and z , respectively; K_0 and K_1 are the modified Bessel functions of the second kind of order 0 and 1, and $\rho = \sqrt{(x-x')^2 + [t(x)-t(x')]^2}$. In the derivation, we have used the following Fourier transform pairs (Equations 3.754 and 3.961 in Gradshteyn and Ryzhik, 1980),

$$\begin{aligned} \int_{-\infty}^{+\infty} \frac{e^{-ik_y y}}{r} dy = \int_{-\infty}^{+\infty} \frac{\cos(k_y y)}{r} dy = 2K_0(\rho|k_y|), \\ \int_{-\infty}^{+\infty} \frac{e^{-ikr} e^{-ik_y y}}{r} dy = \int_{-\infty}^{+\infty} \frac{e^{-ikr} \cos(k_y y)}{r} dy \\ = 2K_0(\rho\sqrt{k_y^2 + i\omega\mu\sigma}), \end{aligned}$$

where $r = \sqrt{(x-x')^2 + y^2 + [t(x)-t(x')]^2}$.

The primary field due to a magnetic dipole can be analytically transformed into the wavenumber domain (Liu, 1989). Thus the right-hand sides of equations (5) and (6) are known.

NUMERICAL COMPUTATIONS

We have carried out numerical computations for a medium with 2-D surface relief. In this case, the fictitious current \mathbf{J} has two components J_y and J_S on the surface S . Here J_y is the component along the y -direction and J_S is the tangential component perpendicular to the y -direction. Equations (5) and (6) can then be written in scalar form as,

$$\begin{aligned} \alpha_i(x, k_y) + \frac{1}{2\pi} \sum_{j=1}^3 \left\{ \int_{-\infty}^{+\infty} \alpha_j(x', k_y) f_{ij}(x, x', k_y) dx' \right\} \\ = \frac{1}{2\pi} \beta_i(x, k_y) \quad (i = 1, 2, 3). \end{aligned} \quad (9)$$

Here,

$$\begin{aligned} \alpha_1(x, k_y) &= \xi(x, k_y), \\ \alpha_2(x, k_y) &= J_y(x, k_y), \\ \alpha_3(x, k_y) &= J_S(x, k_y), \\ f_{11}(x, x', k_y) &= -(V_x n_x + V_z n_z), \\ f_{12}(x, x', k_y) &= U_z n_x - U_x n_z, \\ f_{13}(x, x', k_y) &= U_y(-n_x \sin \theta + n_z \cos \theta), \\ f_{21}(x, x', k_y) &= -(V_x n_z + V_z n_x), \\ f_{22}(x, x', k_y) &= U_x n_x + U_z n_z, \\ f_{23}(x, x', k_y) &= -U_y(n_z \sin \theta + n_x \cos \theta), \\ f_{31}(x, x', k_y) &= -V_y, \\ f_{32}(x, x', k_y) &= 0, \\ f_{33}(x, x', k_y) &= U_x \sin \theta - U_z \cos \theta, \\ \beta_1 &= -n_x H_{px}(x, k_y) + n_z H_{pz}(x, k_y), \\ \beta_2 &= -n_z H_{px}(x, k_y) + n_x H_{pz}(x, k_y), \\ \beta_3 &= -H_{py}(x, k_y), \end{aligned}$$

where θ is the angle between the x -axis and the tangential in the x - z plane at point $P(x', y')$; n_x , n_y , and n_z are the directional cosines of the unit vector \mathbf{n} at the point $M(x, y, z)$; U_x , U_y , and U_z are the three components of \mathbf{U} and V_x , V_y , and V_z are the three components of \mathbf{V} .

To solve the three-coupled integral equations (9) numerically, the infinite integration interval must be truncated. This finite computational domain can then be discretized into N small elements with a node in each element. The element boundary is at the midpoint between two nodes. Here, we use a quadratic interpolation function to approximate the behavior of the charge and current densities inside each element. The coefficients of the quadratic function in each element are determined from the values at its node and two

neighboring nodes (Parry and Ward, 1971). Note here that the nodes are usually nonuniformly spaced and the element size depends on its distance from the source. Integrating the contributions of every element in equation (9), we obtain a system of complex linear equations for the node values,

$$\mathbf{K}\alpha = \mathbf{B}. \quad (10)$$

Here \mathbf{K} is the $3N \times 3N$ coefficient matrix assembled from the element integrals. Each component of the matrix has contributions from three neighboring elements; α is a column vector of the unknown charge and current densities at every node; and \mathbf{B} is a column vector of the known boundary values, β , on the surface S .

Equations (10) are solved independently for each of fifteen wavenumbers. The wavenumber k_y is sampled on a logarithmic scale with five points per decade. Except for its initial value of 0, k_y ranges from 10^{-3} to 1. Once the charge density is obtained, the horizontal and vertical components of the secondary magnetic field in the air can be computed in k_y space from the following equations which are the Fourier transformation of equation (3),

$$H_{sx}(x, k_y, z) = 2 \int_{-\infty}^{+\infty} (x - x') f(x, x', k_y, z) dx' \quad (11)$$

and

$$H_{sz}(x, k_y, z) = 2 \int_{-\infty}^{+\infty} (z - t(x')) f(x, x', k_y, z) dx', \quad (12)$$

where the integration kernel is

$$f(x, x', k_y, z) = \xi(x', k_y) \sqrt{1 + [dt(x')/dx']^2} \frac{|k_y|}{R} K_1(R|k_y|) dx',$$

$$R = \sqrt{(x - x')^2 + [z - t(x')]^2}$$

We now need to take the inverse Fourier transform to get the required final results. Prior to performing this operation however, the field values at logarithmically spaced points in the k_y space need to be interpolated to a uniform grid using cubic spline interpolation.

VERIFICATION OF NUMERICAL PROCEDURES

Flat conductive half-space

An initial check of the numerical computation can be obtained by considering the case of a conductive half-space with a flat surface. In this case the analytical solution in an integral form is well known (Ward and Hohmann, 1987) so that the numerical results can be verified for a wide range of frequencies. We first consider the response of a helicopter-

towed electromagnetic (HEM) system. The transmitter is a small coil driven with an alternating electric current and is located 30 m above the ground. The receiver is an induction coil that measures the secondary magnetic field. The transmitter and receiver coils can be taken as coaxial horizontal dipoles and are separated by 6.5 m. The ground is assigned a conductivity value of 0.1 S/m. The grid used in the computation is shown in Table 1.

The coaxial system response obtained at the center of the computational domain, which is 354 m wide, is plotted in Figure 2. The abscissa indicates the in-phase component of the secondary magnetic field expressed in parts per million (ppm) of the received primary magnetic field while the ordinate is the quadrature component. In the illustration, the circles represent the numerical solution while the solid line is the analytical solution. As shown, the numerical result agrees well with the analytical solution over the entire 25 Hz to 250 kHz frequency range. In fact, except at 25 Hz, the error of the numerical solution for both the in-phase and quadrature components is, in this case, less than 1 percent at any indicated frequency. The relative error of the numerical solution increases with decreasing frequency. This problem is caused by the theoretical formulation that breaks down when the frequency approaches zero. A similar problem was also observed by Doherty (1988).

Conductive valley

The numerical solution was also checked on a laboratory scale model of a valley. Aluminum was used to simulate the conductive terrain at a dimension scale of 1:250. A model airborne electromagnetic system was built at the same scale and was "flown," for experimental convenience, at a field height of 10 m (4 cm in the laboratory). The frequency scale of the model is 1:3750 while the conductivity scale is $2.34 \times 10^8:1$. The system consisted of a coplanar, vertical axis transmitter and receiver, which were operated at a field frequency of 150 kHz (40 Hz in the laboratory) and were separated by a field distance of 10 m. The conductivity of the aluminum used in our experiment is 2.34×10^7 S/m, which simulates a ground conductivity of 0.1 S/m. Note that the

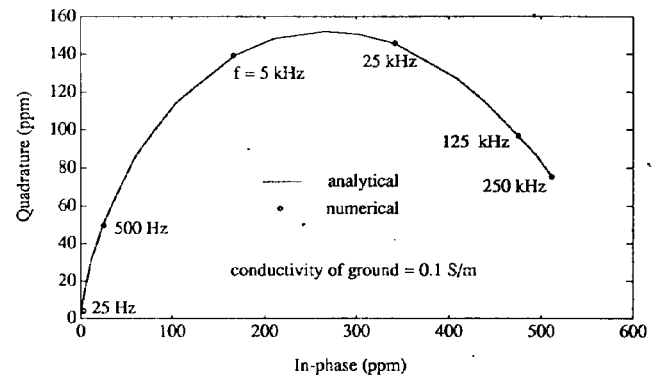


FIG. 2. Comparison of numerical and analytical AEM response (coaxial) over a flat ground of 0.1 S/m. System altitude = 30 m.

Table 1. Typical grid used for numerical computation.

| Cell No. | 1-3 | 4-8 | 9-16 | 17-32 | 33-40 | 41-45 | 46-48 |
|----------------|-----|-----|------|-------|-------|-------|-------|
| Δx (m) | 20 | 9 | 6 | 3 | 6 | 9 | 20 |

model parameters are related to the field parameters by the following equation (Frischknecht, 1987),

$$\sigma' f' \ell'^2 = \sigma f \ell^2.$$

Here σ , f , and ℓ are the field conductivity, frequency, and dimension, while the notation with a prime represents the corresponding model parameter.

The cross-section of the simulated valley, shown in Figure 3, is a Gaussian function given by

$$t(x) = A \exp\left(-\frac{x^2}{0.361W^2}\right). \quad (13)$$

Here,

x = distance from the valley center line

t = topographic relief

A = valley depth

W = valley width at mid depth.

The shape of the valley is invariant along the strike direction. For the model valley, A and W were taken to be 3.4 m and 21 m, respectively. The measurements and numerical calculation results for this model are also displayed in Figure 3 for the in-phase and quadrature components of the secondary magnetic field. Here the system response is plotted at a point located midway between the transmitter and receiver. The measurement error in the experiment is estimated to be less than 5 percent for the in-phase component and 10 percent for

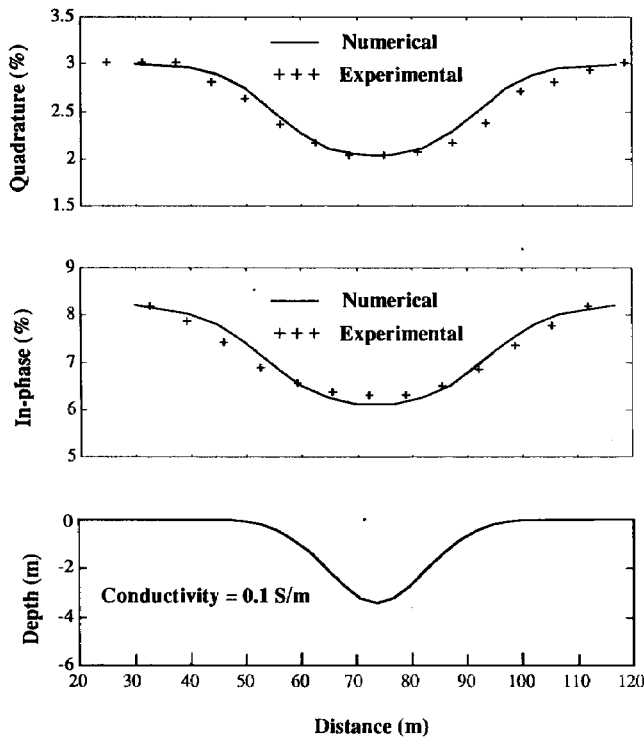


FIG. 3. Comparison of numerical and experimental results for a Gaussian model valley. The simulated coplanar system is flown at an altitude of 10 m with an operation frequency of 150 kHz.

the quadrature component. Within these limits, the numerical and experimental data agree well.

TERRAIN EFFECTS

Here we present numerical results for AEM surveys made over escarpment, valley, and hill models. The AEM system simulated in this study includes the coaxial and coplanar coil configurations. The transmitter and the receiver are separated by 6.5 m. The operation frequency is 8 kHz and the conductivity of the ground is assumed to be 0.1 S/m. Since the response of the coplanar system resembles that of the coaxial system, we will concentrate on the analysis of the results for the coaxial system. The grid used in the computation is identical to that used previously (Table 1).

Escarpment

Let us first consider a smooth escarpment model whose relief is given by

$$t(x) = \frac{b}{\pi} \left(\frac{\pi}{2} + \tan^{-1}(ax) \right),$$

where b is the elevation at the top of the escarpment and a is related to its slope; x is the distance from the center of the escarpment. The survey is flown at constant barometric elevation so that the system coils are maintained at $z = -30$ m or 30 m above the upper level of the feature.

Figure 4 shows the coaxial response for an escarpment defined by $a = 0.1309$ and $b = 24$ m. The slope is 45 degrees at the center of the escarpment. Both the in-phase

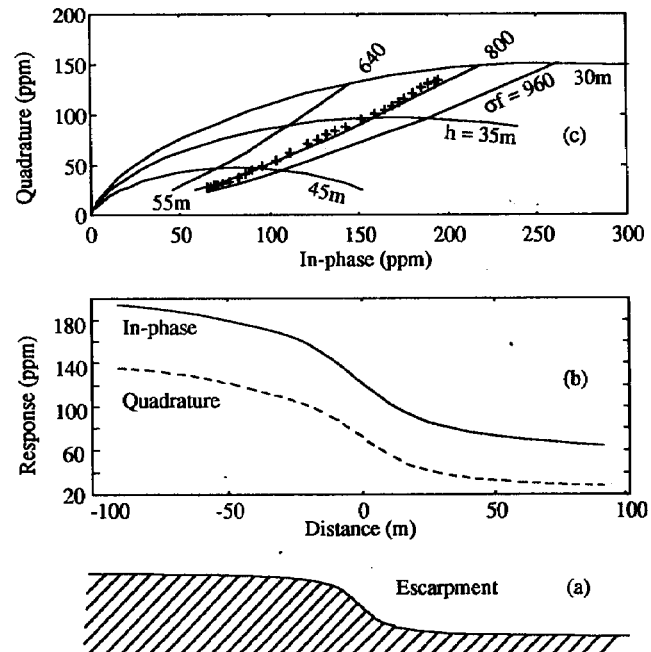


FIG. 4. (a) Model escarpment. (b) Numerical coaxial AEM response over the model escarpment. The system is flown at 30 m above the upper level of the escarpment. (c) Argand diagram of the response (crosses); background lines are the AEM response over a flat ground surface.

and the quadrature vary smoothly over the escarpment as expected (Figure 4b). At either side, the influence of the escarpment may be neglected at a distance of twice the system height. Although the escarpment is antisymmetric about $x = 0$, the response is asymmetric since the response is nonlinear with the system height.

To examine the effects of the escarpment on a conventional method of data interpretation in terms of an apparent resistivity (Fraser, 1978), we have replotted the profile data on an Argand chart of conductive half-space response. As can be seen in Figure 4(c), the data points are very closely aligned with the $\sigma f = 800$ radial. Given the 8 kHz frequency for the numerical experiment, all the data for this profile will yield the correct apparent resistivity of 0.1 S/m.

Valley

The simulation is done for an overflight of a symmetric triangular valley with 20-degree side slopes and a base width of 120 m. The system flight height is maintained at a constant altitude of 30 m above the flat part of the terrain. In this case, as shown in Figure 5, both the in-phase and quadrature components of the secondary field show a negative anomaly over the valley. Its amplitude is about 100 ppm in the in-phase component and about 85 ppm in the quadrature secondary field.

Again we have replotted the profile data on an Argand chart of conductive half-space response. As can be seen in Figure 5(c), all the data for this profile will also yield the

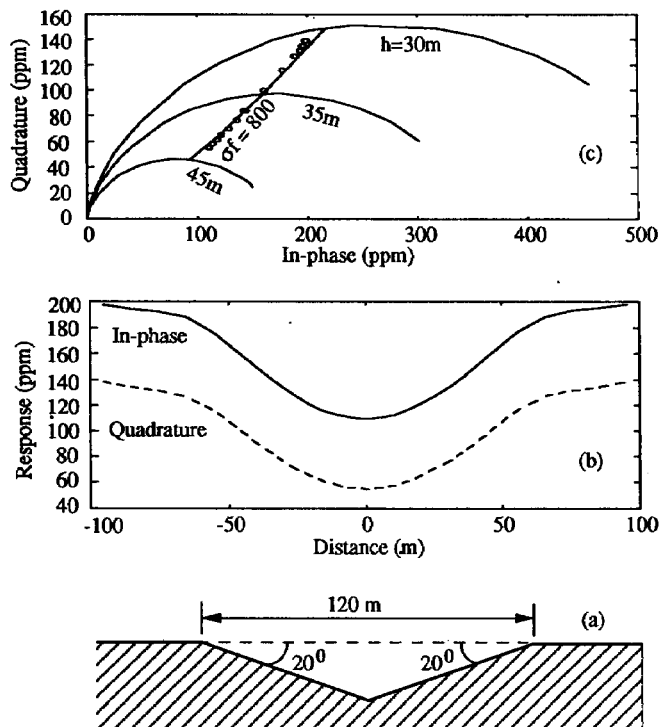


FIG. 5. (a) Model valley. (b) Numerical coaxial AEM response over the model valley. The system is flown at 30 m above the flat part of the terrain. (c) Argand diagram of the response (circles); background lines are the AEM response over a flat ground surface.

correct apparent resistivity of 0.1 S/m. Numerical experiments at other frequencies (1 and 64 kHz) yield similar results. It thus appears that the phase of the secondary field is not affected much by terrain features over a fairly wide range of operating frequencies.

The presence of the valley, however, is clearly indicated by the incorrect estimate of the system height above the conducting surface in Figure 5(c). This quantity turns out to be 43 m over the deepest portion of the valley which in fact lies at about 52 m below the AEM system. This incorrect estimate of the system elevation is caused by using the flat ground model in the case of a ground with terrain relief.

Hill

We now examine the numerical results that would be obtained in a overflight of a small, symmetric, triangular hill with a base width of 60 m and slopes of 20 degrees. In this case the aircraft altitude is maintained at 30 m above the terrain including the hill summit that rises 11 m above the background. The results for this draped overflight simulation are shown in Figure 6. This time the signal amplitude rises somewhat as we approach the hill and then falls sharply when the aircraft altitude is raised to maintain constant terrain clearance over the hill top. Once again, when the numerical results are plotted on the appropriate Argand diagram, a correct value of apparent resistivity is indicated all along the profile. The apparent system terrain clearance

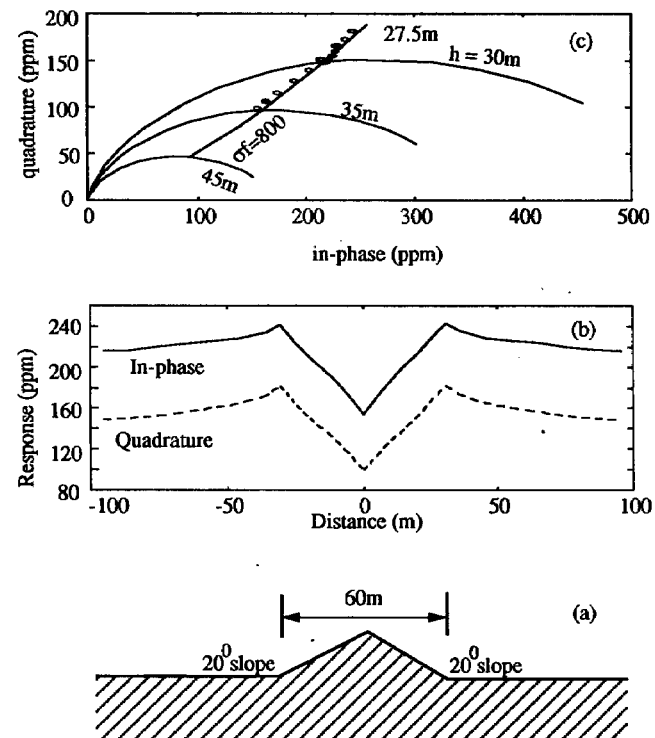


FIG. 6. (a) Model hill. (b) Numerical coaxial AEM response over the model hill. The system is flown at a constant terrain clearance of 30 m including the hill summit. (c) Argand diagram of the response (circles); background lines are the AEM response over a flat ground surface.

however is in error as it indicates a system altitude of 35 m [Figure 6(c)] over the hill top.

CONCLUSIONS

The numerical results show that frequency domain AEM data acquired in areas of moderate topography can be interpreted using the conventional Argand diagram method to obtain good estimates of ground conductivity. Because the system footprint is of the same order of magnitude as its elevation above ground surface, the secondary field amplitude is not affected by any topography that is distant from the AEM system by more than twice the system elevation. Directly overflown features will, however, affect the observed secondary field amplitude. This effect can be ignored in obtaining conductivity estimates for a homogeneous half-space but could lead to erroneous estimates in areas where the ground exhibits layering.

One should note however that not all possible "apparent conductivity" definitions will yield this satisfactory result. In the Argand diagram method used above, the interpreted conductivity value is closely related to the phase angle of the secondary field and this quantity does not show much variation with terrain clearance. On the other hand, Fraser (1978) shows that one can also obtain reliable conductivity estimates by considering the amplitude of the secondary field for a given terrain clearance. This method will not give proper results over irregular terrain and will introduce terrain effects into the conductivity estimates. For example, if we consider the synthetic survey results for the escarpment (Figure 4), we see a very noticeable change in secondary field amplitude at some distance from the escarpment slope that is not accompanied by any visible change in terrain clearance. Use of the "altitude-amplitude" method here would result in a severe (50 percent) underestimation of the terrain conductivity near the upper level of the escarpment.

Finally, we would like to suggest other uses for the 2-D algorithm presented here. It can also be used to model the effects of a conductive basement under a resistive overburden of variable thickness. A practical application of this concept is the computation of AEM low-frequency response of the irregular interface between sea ice and sea water in the Arctic regions. The previously published work in this area

(Liu and Becker, 1990) was based on the assumption that the system response was at the inductive limit so that the conductivity of the sea water could be considered to be infinite.

ACKNOWLEDGMENT

The analytical solution shown in Figure 2 was computed with program EM1D written by Dr. Ki Ha Lee. We also thank G. R. Olhoeft, S. A. Arcone, and an anonymous reviewer for helpful reviews of this paper. Partial funding for this work was provided by the U.S. Geological Survey.

REFERENCES

- Arcone, S. A., 1978, Investigation of a VLF airborne resistivity survey conducted in northern Maine: *Geophysics*, **43**, 1399-1417.
- Brebbia, C. A., Telles, J. C. F., and Wrobel, L. C., 1984, *Boundary element techniques—Theory and applications in engineering*: Springer-Verlag, New York, Inc.
- Doherty, J., 1988, EM modeling using surface integral equations: *Geophys. Prosp.*, **36**, 644-668.
- Eberle, D., 1981, A method of reducing terrain relief effects from VLF-EM data: *Geoexpl.*, **19**, 103-114.
- Fraser, D. C., 1978, Resistivity mapping with an airborne, multicoil, electromagnetic system: *Geophysics*, **43**, 144-172.
- , 1979, The multicoil II airborne electromagnetic system: *Geophysics*, **44**, 1367-1394.
- Frischknecht, F. C., 1987, Electromagnetic physical scale modeling, in Nabighian, M. N., Ed., *Electromagnetic methods in applied geophysics—Vol. 1, Theory*: Soc. Expl. Geophys.
- Gradshteyn, I. S., and Ryzhik, I. M., 1980, *Table of integrals, series, and products*: Academic Press Inc.
- Harrison, R. P., Hecksher, J. L., and Lewis, E. A., 1971, Helicopter observations of very low frequency waves over certain mountains and shore lines: *J. Atmos. and Terrest. Phys.*, **33**, 101-110.
- Karous, M. R., 1979, Effects of relief in EM methods with very distant source: *Geoexpl.*, **17**, 33-42.
- Liu, G., 1989, Airborne electromagnetic sensing of sea ice thickness: Ph.D. dissertation, Univ. of California at Berkeley.
- Liu, G., and Becker, A., 1990, Two-dimensional mapping of sea ice keels with airborne electromagnetics: *Geophysics*, **55**, 239-248.
- Mayergoyz, I., 1982, Boundary integral equations of minimum order for the calculation of three-dimensional eddy current problems: *IEEE Trans. on Magnetics*, **Mag-18**, 536-539.
- Parry, J. R., and Ward, S. H., 1971, Electromagnetic scattering from cylinders of arbitrary cross-section in a conductive half-space: *Geophysics*, **36**, 67-100.
- Ward, S. H., and Hohmann, G. W., 1987, Electromagnetic theory for geophysical applications, in Nabighian, M. N., Ed., *Electromagnetic methods in applied geophysics—Vol. 1, Theory*: Soc. Expl. Geophys.
- Whittles, A. B. L., 1969, Prospecting with radio frequency EM-16 in mountainous regions: *Western Miner*, **42**, 51-56.